Electron Ghost Imaging

S. Li, F. Cropp, K. Kabra, T. J. Lane, G. Wetzstein, P. Musumeci, and D. Ratner

Phys. Rev. Lett. **121**, 114801 — Published 11 September 2018

DOI: 10.1103/PhysRevLett.121.114801

Electron ghost imaging

S. Li,[1] F. Cropp,[2] K. Kabra,[2] T.J. Lane,[1] G. Wetzstein,[3] P. Musumeci,[2] and D. Ratner[1]

[1] *SLAC National Accelerator Laboratory, Menlo park, California, 94025, USA*
[2] *Department of Physics and Astronomy, UCLA, Los Angeles, California 90095, USA*
[3] *Stanford University, Stanford, California, 94305, USA*

In this letter we report a demonstration of electron ghost imaging. A digital micromirror device directly modulates the photocathode drive laser to control the transverse distribution of a relativistic electron beam incident on a sample. Correlating the structured illumination pattern to the total sample transmission then retrieves the target image, avoiding need for a pixelated detector. In our example, we use a compressed sensing framework to improve the reconstruction quality and reduce the number of shots compared to raster scanning a small beam across the target. Compressed electron ghost imaging can reduce both acquisition time and sample damage in experiments for which spatially resolved detectors are unavailable (e.g. spectroscopy) or in which the experimental architecture precludes full frame direct imaging.

Classical ghost imaging (GI) (e.g. [1]) is a method to extract spatially-resolved sample characteristics from single pixel detectors. Classical GI (also known as the "single pixel camera" in computational imaging, see e.g. [2]) reconstructs a sample's spatial properties by correlating the measured structured transverse distribution of the illuminating beam to a "bucket" (single pixel) measurement of the sample response. This imaging modality is especially useful when pixelated detectors are unavailable or the experimental architecture precludes full frame imaging. In recent years GI has been applied to a growing range of illumination types, including both x-rays [3–5] and atoms [6]. Despite theoretical studies [7, 8], to date there have been no experimental demonstrations of electron ghost imaging.

Potential benefits of applying ghost imaging methods to electron-based imaging systems include the possibility to minimize image acquisition time and to reduce the dose delivered to the sample and the resulting sample damage [9, 10]. In addition, electron ghost imaging can be useful for experimental methods (e.g. electron energy-loss spectroscopy [11], or cathodoluminescence [12]) for which spatially resolved detectors either do not exist or severely increase the complexity of the setup. A special case is the growing field of time-resolved electron scattering where the use of multi-MeV, ultrashort relativistic electron sources for both imaging and diffraction has pushed temporal resolution to the ps and fs regimes [13–15]. Employing structured illumination (i.e. ghost imaging) schemes on ultrashort electron beams offers the possibility to better manage the space charge effects in the electron column.

Conventional GI splits the illumination in two paths to allow for the measurement of the transverse profile while only a fraction of the main beam (the "ghost") samples the target. Even though very low energy electron beam splitters are being developed [16, 17], at energies commonly employed in electron scattering instruments (> 10 keV) there is no practical solution for splitting the beam and upstream measurements of the transverse beam profile would affect the distribution incident on the sample. Fortunately, a variation of GI known as computational ghost imaging [18] avoids the need for direct measurement by explicitly controlling the distribution of the incident illumination. For example, in [18] a spatial light modulator was employed to pattern the wavefront, and this known pattern was correlated to the bucket detector without any additional measurement. Similar control is possible with electrons; modulating the shape of a photocathode drive laser controls the emitted electron beam [19, 20], enabling computational GI with electrons. Using a relativistic multi-MeV electron beam has the significant advantage of reducing space charge effects, improving preservation of the electron beam structure during transport from the cathode to the sample.

In this letter, we report an experimental demonstration of computational electron GI using a high-brightness relativistic electron beam (3.2 MeV) from a radiofrequency (RF) photoinjector. In our proof-of-principle, we reproduce a target image by correlating the total electron transmission through the sample with the programmed patterns of a digital micromirror device (DMD). In the reconstruction we use compressed sensing [21, 22] to reduce the total number of shots, improving speed of acquisition and reducing sample exposure. (See e.g. [23] for other applications of compressed sensing to scanning electron microscopy.) The considerable freedom in structuring the transverse illumination profile, enabled by the DMD, allows us to test and compare two different sets of illumination patterns: raster scanning by turning on a single DMD (macro)pixel at a time, compared to turning on a randomized fraction ($\sim$50 %) of the pixels for each mask (multipixel, or MP).

The experiment was carried out at the UCLA Pegasus beamline [24] where a 0.8 ps RMS 266 nm laser pulse illuminates a Cu cathode in the high field S-band 1.6 cell RF gun to generate the electron beam. The initial electron beam profile at the cathode can be controlled by applying a mask to the transverse profile of the drive laser pulse. For the shaping we used a TI DLP-7000 DMD, with a

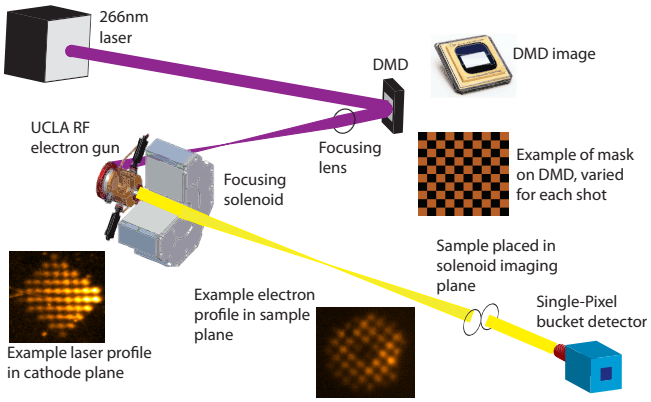

FIG. 1. Schematics of the ghost imaging experiment. An ultrashort 266 nm laser pulse illuminates the DMD and is then imaged onto the cathode. The generated electron beam is imaged using the gun solenoid onto a target located 2.7 m downstream. A single pixel bucket detector records the intensity of the transmitted beam after the target. The reduced intensity in the center of the electron profile is due to the cathode's nonuniform quantum efficiency.

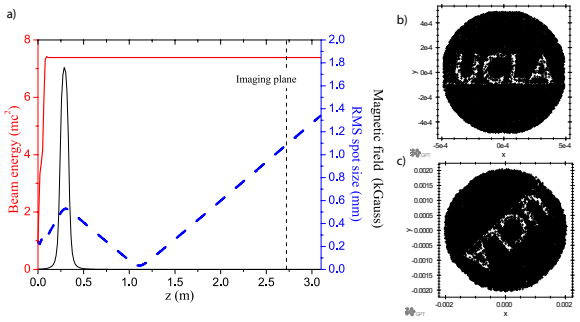

FIG. 2. Evolution of beam energy and rms spot size along the beamline. The longitudinal component of the magnetic field of the solenoid lens is also shown. The "UCLA" shape impressed by the DMD on the photoemission laser pulse (b) is imaged with a rotation angle determined by the solenoid (c). This angle is taken into account in the reconstruction analysis.

modified window to allow ultraviolet (UV) transmission, as discussed in [20]. An 80 cm focal length lens imaged the DMD onto the cathode with demagnification factor 0.2 (Fig. 1), and an 1800 lines/mm diffraction grating compensated the pulse front tilt introduced by the mirror array. A 5 mm laser spot on the DMD fully illuminated a region of 160×160 pixels on the array. To reduce the experimental complexity, we defined "macropixels" made of 8×8 or 16×16 squares of physical DMD pixels. The input UV laser energy was limited to $< \ 10\ \mu$J to avoid DMD damage [25]. Due to significant losses on the grating, DMD, and transport line, less than 5% of the input UV energy reached the cathode. The maximum charge per pulse used in the experiment was 250 fC. A virtual cathode camera monitored the laser profile, and a remotely controlled lens translation stage fine-tuned the imaging condition.

After the RF gun [26], the 3.2 MeV kinetic energy electron beam was focused using a 1.9 kG field solenoid lens (effective length 20 cm) located 29 cm downstream of the cathode and imaged to a 4 mm diameter spot (magnification = 4) on the target plane, at a distance of 2.7 m from the cathode. Even for the very low peak currents (< 1 Amp) and charge densities (< 0.1 pC/mm^2) used in this experiment, space charge had non-negligible effect on the beam dynamics, and in particle tracking simulations it is observed to contribute to the resolution limit in the electron imaging system, with the other main effects being the chromatic aberrations of RF and solenoid fields (Fig. 2). For the conditions of the experiment, it was found (in agreement with the simulations) that features on the cathode of less than 100 μm size were significantly blurred at the target plane. No attempts were made in trying to improve the spatial resolution, as it was not the goal of these first experiments. Nevertheless, we note that a multi-lens electron imaging system could be used to demagnify the cathode transverse profile by large factors to improve the spatial resolution of the technique.

A fluorescent screen (13 cm downstream, DRZ$^{\rm TM}$), imaged with a standard CCD camera, was placed at the target plane to measure the electron transport and imaging condition. The transport was assumed to stay constant throughout the experiment and was measured only once prior to inserting the target.

After inserting a target, Fig. 3, into the beam, the transmitted electrons were collected on the DRZ screen, directly behind the target. In post analysis of each DRZ image, we remove all background and select only the photo-emitted electron beam region. Finally, integrating the signal over the selected region on the DRZ screen yields the single-pixel "bucket-detector." Two main sets of DMD configurations were recorded: a multipixel random set in which each of the DMD macropixels (either 8×8 or 16×16 actual pixels) was turned on with 50% probability and a raster set in which only one macropixel (16×16 actual pixels) of the DMD was turned on for each pattern.

Early GI experiments reconstructed the target image via a direct correlation of the incident pattern and bucket detector. However, it is also possible to pose GI as an image formation problem and make use of well established optimization methods, such as compressed sensing [21, 22]. The measurement can be written as a dot product,

$$b^{(i)} = \sum_{m,n} A^{(i)}_{mn} x_{mn} \qquad (1)$$

where x_{mn} is the unknown (two-dimensional) sample image, while $A^{(i)}_{mn}$ is the ith pattern applied to the DMD, $b^{(i)}$

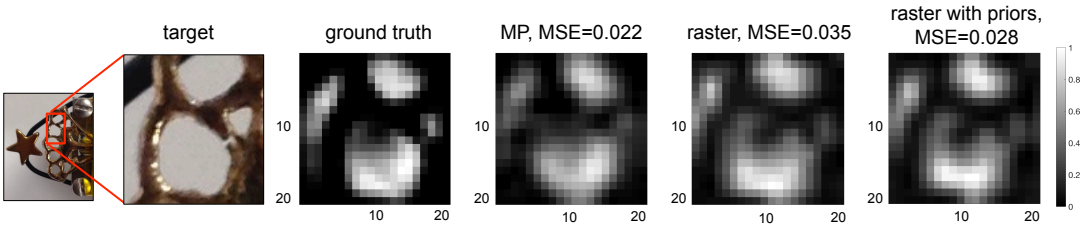

FIG. 3. From left to right, we show an optical photo of the target, the constructed ground truth electron transmission image, the best reconstruction from the MP data set, a 10×10 raster scan interpolated to 20×20 pixels, and a 10×10 raster scan solved with Eq. 2 on a 20×20 grid. Note that the ground truth is the product of the object transmission and cathode QE.

is the summed intensity on the bucket detector for pattern i, and m, n are the indices of the sample image and DMD macropixels. Note that in practice, x_{mn} will represent the ground truth combined with machine systematics, such as the cathode quantum efficiency (QE). With $N_p = m \times n$ macropixels on the DMD and combining data from N_s shots, we can reshape $A^{(i)}_{mn}$ into a $N_s \times N_p$ matrix $\boldsymbol{A}$, x_{mn} into a N_p long vector $\boldsymbol{x}$, and $b^{(i)}$ into a N_s long vector $\boldsymbol{b}$. In our example, each "bucket" measurement $b^{(i)}$ is a scalar, but the same formalism works for more general measurements, e.g. a lineout from a spectrometer.

To solve Eq. 1 for $\boldsymbol{x}$, we use the alternating direction method of multipliers (ADMM), a standard convex optimization tool used in image reconstruction that allows the flexibility of including prior knowledge of the physical system into the solution [27]. To apply ADMM to the electron GI experiment, we add priors to Eq. 1, and rewrite as a constrained optimization problem,

$$\begin{aligned} \underset{x}{\text{minimize}} \quad & \frac{1}{2}||\boldsymbol{A}\boldsymbol{x} - \boldsymbol{b}||_2^2 + \lambda_1||\boldsymbol{z_1}||_1 + \\ & \text{Ind}_+(\boldsymbol{z_2}) + \lambda_2||\boldsymbol{z_3}||_2^2 \\ \text{subject to} \quad & \boldsymbol{K}\boldsymbol{x} - \boldsymbol{z} = 0, \boldsymbol{K} = \begin{pmatrix} \boldsymbol{I} \\ \boldsymbol{I} \\ \boldsymbol{L} \end{pmatrix}, \boldsymbol{z} = \begin{pmatrix} \boldsymbol{z_1} \\ \boldsymbol{z_2} \\ \boldsymbol{z_3} \end{pmatrix}. \end{aligned} \tag{2}$$

Besides the quadratic term which minimizes the difference between the reconstruction and the measurement, we consider three priors based on the sample type: sparsity to favor large areas of background, non-negativity to ensure non-negative sample transmission, and smoothness to favor round edges and remove speckles. These constraints are included in the minimization problem using the auxiliary (slack) variables $\mathbf{z}_{1-3}$. The Laplacian operator $\boldsymbol{L}$ implementing the finite difference approximation of the second derivative enforces smoothness. The indicator function Ind_+ is infinite when the argument is negative and $||\mathbf{y}||_1$ and $||\mathbf{y}||_2$ represent the $L1$ and $L2$ norms of vector $\mathbf{y}$. The ADMM implementation alternatively treats each of the $(\boldsymbol{x}, \boldsymbol{z_{1-3}})$ variables as the only independent variable while keeping the others fixed, which iteratively approaches a solution satisfying the stated constraints.

The hyper-parameters $\lambda_{1,2}$ in Eq. 2 determine the relative weight of the corresponding priors. To choose hyper-parameters, we conduct a simulation by applying the macropixel size, experimentally measured noise level, cathode QE map, and beam jitter to a ring pattern with similar diameter and thickness as the physical target. After optimizing hyper-parameters with the simulation, we keep parameters fixed for analysis of experimental data.

We collected data sets with two different DMD patterns: raster and multipixel (MP) random masks. The raster data set consists of 100 patterns, with a single macropixel in a 10×10 grid turned on for each pattern. (Each macropixel consists of 16×16 physical pixels on the DMD.) The two MP data sets consist of 400 distinct patterns (for a 20×20 grid with 8×8 pixels per macropixel) and 326 patterns (for a 10×10 grid with 16×16 pixels per macropixels). For each MP pattern, macropixels were masked independently with a 50% probability, equivalent to a random Bernoulli matrix with $p = 0.5$. To improve signal-to-noise, for each pattern we averaged multiple shots (5 for MP, 10 for raster) to generate the bucket value.

To create the ground truth image, we record a DRZ detector image of the sample with all DMD pixels turned on. We then rotate the DRZ image to compensate for the solenoid rotation (Fig. 2). The resulting image represents an electron transmission image of the sample, scaled by the cathode QE. (Note that space charge effects will blur small QE features.) This is the same measurement we expect to reconstruct with the ghost imaging analysis. We assess the quality of the reconstruction with the mean squared error (MSE),

$$\text{MSE} = \frac{1}{MN}\sum_{m=1}^{M}\sum_{n=1}^{N}\left(T_{mn} - x_{mn}\right)^2, \tag{3}$$

where T_{mn} is the ground truth, and x_{mn} is the reconstructed two dimensional sample image. The smoothness prior alone is able to reduce MSE by 27% and 21% for MP 20×20 and MP 10×10. Just as for the MP data set, we can apply Eq. 2 to the rastered data set to include priors in the solution; for example, applying the

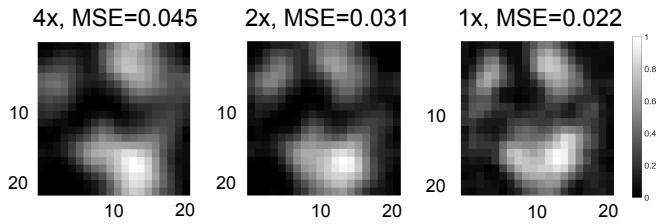

FIG. 4. Reconstruction results for the MP 20×20 data sets with compression factor being 4, 2, and 1.

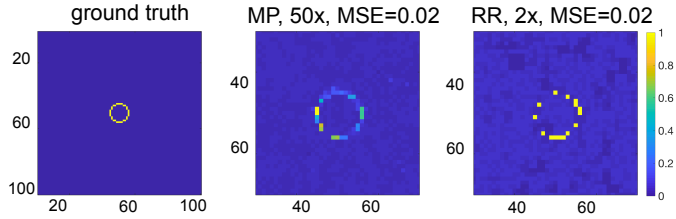

FIG. 5. Simulation of MP and RR reconstruction for a 100 × 100 image. Left: ground truth image. Middle: MP, SNR = 200, compression factor of 50, MSE = 0.02. Right: RR, SNR = 200, compression factor of 2, MSE = 0.02. The reconstructions are zoomed in to present a clearer view of the reconstruction quality. The MSE is calculated in a 30×30 pixel region centered around the sample.

smoothness prior reduces MSE by 21%. Figure 3 shows the ground truth image and the best reconstructions from the different methods.

To assess the impact of compressed sensing on the data acquisition rate, we performed reconstructions with increasingly smaller subsets of the total dataset. The compression factor is defined as the total number of macropixels divided by the number of patterns used for reconstruction. With this definition, a full raster scan has compression factor of 1. We run the reconstruction for the 20 × 20 MP data set with compression factors of 1, 2, and 4. The results are given in Fig. 4.

In our simple proof-of-principle, Fig. 3 shows that both MP and rastering can reproduce the sample shape. Given that rastering can be accomplished by focusing and sweeping the beam, it is interesting to ask whether the DMD is necessary. In general, the choice between MP and rastering for future experiments will depend on the experimental conditions and sample type. In MP, the beam charge is spread across multiple macropixels, while in rastering only a single macropixel is illuminated per shot, so if charge density is the same, each MP shot results in higher dose to the sample. Consequently, for experiments limited by sample damage and with good SNR, rastering may be preferable to MP. Conversely, when acquisition time is important, MP can resolve a target with relatively few and small features with higher compression factor, resulting in faster acquisition time than rastering.

To illustrate the trade-off, we simulate an experiment using both rastering and MP to reconstruct a sparse sample while minimizing either acquisition time or sample damage. For a fair comparison, we introduce a "random-raster" (RR) data set, which is a random subset of the patterns in the full raster scan: this allows for compressed sensing in both cases. The simulated target is a small ring with 5 unit radius and 1 unit width on a 100 × 100 unit grid. In total, just 28 out of 10^4 points are non-zero. We find MP reconstructs a reasonable image with just 200 shots (compression factor of 50), while RR requires 5000 shots (compression factor of 2) to reach the same MSE (Fig. 5). However, by illuminating only a single macropixel per shot, the RR approach has a 4-fold lower cumulative dose. (This includes a 50-fold increase in charge density for the RR case to achieve the same SNR, defined as the ratio of fluctuations in signal to fluctuations in noise at the bucket detector). We note that the relative benefits of the two methods will in general depend on experimental constraints, noise sources, sample type, available priors, and even error metric, and should be evaluated on a case-by-case basis. Moreover, the DMD provides the flexibility for a wide range of illumination schemes, e.g. using an arbitrary fraction of macropixels or partial illumination of each macropixel.

This letter reports an experimental demonstration of GI with multi-MeV relativistic electrons. By controlling the electron profile with a DMD in the injector laser path, we reconstruct the sample without measuring the incident beam of each exposure. GI has diverse applications in experiments for which pixelated detectors do not exist (e.g. spectroscopy or cathodoluminescence), or in which the geometry does not permit imaging of the sample. We use the compressed sensing formalism, which reduces acquisition time and risk of sample damage by imposing priors on the reconstruction. While our demonstration used random DMD patterns, the flexibility of the DMD in principle allows the user to select patterns "on-the-fly" to optimally converge to a solution or to tailor the patterns to specific sample priors, further improving the acquisition time and reducing damage.

The ability to impose arbitrary shapes on the electron beam may also enable related imaging methods, for example structured [28] or adaptive [29] illumination. Patterning the beam in momentum space with optics between the photocathode and the sample could enable Fourier ptychography [30]. Although we used MeV electrons, lower energies are possible if the charge density is low enough to avoid distortion from space charge. Finally, computational GI is in principle applicable to all laser-driven particle sources by patterning the drive or photoionizing laser, with examples including laser-based plasma sources [31], cold electron and ion sources [32, 33], laser-driven neutron sources [34], and even laser driven photon sources such as high-harmonic generation [35] and inverse Compton scattering [36]. In each case, practical implementations will depend on the ability to image the

initial transverse laser pattern onto the sample.

We would like to thank Renkai Li for helpful discussions. This work was supported by U.S. Department of Energy Office of Science under Contract No. DE-AC02-05CH11231 and the National Science Foundation under Grant No. DMR-1548924. SL acknowledges support from the Robert H. Siemann Graduate Fellowships in Physics.

[1] B. I. Erkmen and J. H. Shapiro, Advances in Optics and Photonics **2**, 405 (2010).
[2] M. Duarte, M. Davenport, D. Takhar, J. Laska, T. Sun, K. Kelly, and R. Baraniuk, IEEE Signal Proc. Mag. **25**, 83 (2008).
[3] D. Pelliccia, A. Rack, M. Scheel, V. Cantelli, and D. M. Paganin, Phys. Rev. Lett. **117**, 113902 (2016).
[4] H. Yu, R. Lu, S. Han, H. Xie, G. Du, T. Xiao, and D. Zhu, Phys. Rev. Lett. **117**, 113901 (2016).
[5] A.-X. Zhang, Y.-H. He, L.-A. Wu, L.-M. Chen, and B.-B. Wang, Optica **5**, 374 (2018).
[6] R. Khakimov, B. Henson, D. Shin, S. Hodgman, R. Dall, K. Baldwin, and A. Truscott, Nature **540**, 100 (2016).
[7] S. Gan, D.-Z. Cao, , and K. Wang, Phys. Rev. A **80**, 043809 (2009).
[8] H.-C. Liu, Phys. Rev. A **94**, 023827 (2016).
[9] R. F. Egerton, Reports on Progress in Physics **72**, 016502 (2008).
[10] J. C. H. Spence, Structural Dynamics **4**, 044027 (2017).
[11] R. K. Li and X. J. Wang, Phys. Rev. Appl. **8**, 054017 (2017).
[12] C. G. Bischak, C. L. Hetherington, Z. Wang, J. T. Precht, D. M. Kaz, D. G. Schlom, and N. S. Ginsberg, Nano Letters **15**, 3383 (2015).
[13] S. Weathersby, G. Brown, M. Centurion, T. Chase, R. Coffee, J. Corbett, J. Eichner, J. Frisch, A. Fry, M. Gühr, *et al.*, Review of Scientific Instruments **86**, 073702 (2015).
[14] D. Cesar, J. Maxson, P. Musumeci, Y. Sun, J. Harrison, P. Frigola, F. H. OShea, H. To, D. Alesini, and R. K. Li, Physical review letters **117**, 024801 (2016).
[15] J. Yang, X. Zhu, T. J. A. Wolf, Z. Li, J. P. F. Nunes, R. Coffee, J. P. Cryan, M. Gühr, K. Hegazy, T. F. Heinz, K. Jobe, R. Li, X. Shen, T. Veccione, S. Weathersby, K. J. Wilkin, C. Yoneda, Q. Zheng, T. J. Martinez, M. Centurion11, and X. Wang1, Science **361**, 64 (2018).
[16] M. M. Dellweg and C. Müller, Physical review letters **118**, 070403 (2017).
[17] P. Kruit, R. Hobbs, C.-S. Kim, Y. Yang, V. Manfrinato, J. Hammer, S. Thomas, P. Weber, B. Klopfer, C. Kohstall, T. Juffmann, M. Kasevich, P. Hommelhoff, and K. Berggren, Ultramicroscopy **164**, 31 (2016).
[18] J. H. Shapiro, Phys. Rev. A **78**, 061802 (2008).
[19] J. Maxson, H. Lee, A. C. Bartnik, J. Kiefer, and I. Bazarov, Phys. Rev. ST Accel. Beams **18**, 023401 (2015).
[20] S. Li, S. Alverson, D. Bohler, A. Egger, A. Fry, S. Gilevich, Z. Huang, A. Miahnahri, D. Ratner, J. Robinson, , and F. Zhou, Phys. Rev. AB **20**, 080704 (2017).
[21] E. J. Candes, J. Romberg, and T. Tao, IEEE Trans. Inf. Theory **52**, 489 (2006).
[22] O. Katz, Y. Bromberg, and Y. Silberberg, Appl. Phys. Lett. **95**, 131110 (2009).
[23] M. D. Guay, W. Czaja, M. A. Aronova, and R. D. Leapman, Scientific Reports **6**, 27614 (2016).
[24] J. Maxson, D. Cesar, G. Calmasini, A. Ody, P. Musumeci, and D. Alesini, Phys. Rev. Lett. **118**, 154802 (2017).
[25] S. Li, D. Bohler, J. Corbett, A. Fisher, S. Gilevich, Z. Huang, J. Robinson, F. Zhou, R. Fiorito, and E. Montgomery, in *Proceedings of IPAC'2015, Richmond, VA, May 3-8, 2015*, pp. 1813–1815.
[26] D. Alesini, A. Battisti, M. Ferrario, L. Foggetta, V. Lollo, L. Ficcadenti, V. Pettinacci, S. Custodio, E. Pirez, P. Musumeci, and L. Palumbo, Phys. Rev. ST Accel. Beams **18**, 092001 (2015).
[27] S. Boyd, N. Parikh, E. Chu, B. Peleato, and J. Eckstein, Foundations and Trends in Machine Learning **3**, 1 (2011).
[28] M. G. Gustafsson, Journal of microscopy **198**, 82 (2000).
[29] L.-H. Yeh, L. Tian, and L. Waller, Biomedical optics express **8**, 695 (2017).
[30] G. Zheng, R. Horstmeyer, and C. Yang, Nature photonics **7**, 739 (2013).
[31] J. Faure, C. Rechatin, A. Norlin, A. Lifschitz, Y. Glinec, and V. Malka, Nature **444**, 737 (2006).
[32] A. McCulloch, D. Sheludko, S. Saliba, S. Bell, M. Junker, K. Nugent, and R. Scholten, Nature Physics **7**, 785 (2011).
[33] M. P. Reijnders, P. A. van Kruisbergen, G. Taban, S. B. vanderGeer, P. H. A. Mutsaers, E. J. D. Vredenbregt, and O. J. Luiten, Physical review letters **102**, 034802 (2009).
[34] J. Alvarez, J. Fernández-Tobias, K. Mima, S. Nakai, S. Kar, Y. Kato, and J. Perlado, Physics Procedia **60**, 29 (2014).
[35] A. LHuillier and P. Balcou, Physical Review Letters **70**, 774 (1993).
[36] S. Chen, N. Powers, I. Ghebregziabher, C. Maharjan, C. Liu, G. Golovin, S. Banerjee, J. Zhang, N. Cunningham, A. Moorti, *et al.*, Physical review letters **110**, 155003 (2013).